COMPUTATIONAL
ANDSTRUCTURAL
BIOTECHNOLOGY
J O U R N A L

Model-based prediction of optogenetic sound encoding in the human cochlea by future optical cochlear implants

Lakshay Khurana [a,b,c,d,e], Daniel Keppeler [a,c,e], Lukasz Jablonski [a,b,e,*], Tobias Moser [a,b,c,e,f,*]

[a] Institute for Auditory Neuroscience, University Medical Center Göttingen, Göttingen, Germany
[b] Auditory Neuroscience and Optogenetics Laboratory, German Primate Center, Göttingen, Germany
[c] Auditory Neuroscience & Synaptic Nanophysiology Group, Max Planck Institute for Multidisciplinary Sciences, Göttingen, Germany
[d] Göttingen Graduate Center for Neurosciences, Biophysics, and Molecular Biosciences (GGNB), University of Göttingen, Göttingen, Germany
[e] InnerEarLab, University Medical Center Göttingen, Göttingen, Germany
[f] Cluster of Excellence "Multiscale Bioimaging: from Molecular Machines to Networks of Excitable Cells" (MBExC), University of Göttingen, Göttingen, Germany

ARTICLE INFO

ABSTRACT

When hearing fails, electrical cochlear implants (eCIs) partially restore hearing by direct stimulation of spiral ganglion neurons (SGNs). As light can be better confined in space than electrical current, optical CIs (oCIs) provide more spectral information promising a fundamental improvement of hearing restoration by cochlear implants. Here, we turned to computer modelling for predicting the outcome of optogenetic hearing restoration by future oCIs in humans. We combined three-dimensional reconstruction of the human cochlea with ray-tracing simulation of emission from LED or laser-coupled waveguide emitters of the oCI. Irradiance was read out at the somata of SGNs. The irradiance values reached with waveguides were about 14 times higher than with LEDs, at the same radiant flux of the emitter. Moreover, waveguides outperformed LEDs regarding spectral selectivity. oCIs with either emitter type showed greater spectral selectivity when compared to eCI. In addition, modeling the effects of the source-to-SGN distance, orientation of the sources and impact of scar tissue further informs the development of optogenetic hearing restoration.

1. Introduction

Disabling hearing loss is the most common sensory deficit affecting about 5% of the world's population [1]. Cochlear implants (CIs) are used by approximately 1 million otherwise deaf or profoundly hearing-impaired people. CIs enable most users to understand speech in quiet environments and are considered the most successful neuroprostheses. An electrical cochlear implant (eCI) converts the sound into electrical pulses, which are delivered to an electrode array in the cochlea of the inner ear. These electrical pulses directly stimulate the spiral ganglion neurons (SGNs) to provide a sense of hearing in the absence of functional sensory hair cells. eCIs capitalize on the tonotopic organization of the cochlea, aiming to recruit different SGNs along the tonotopic (frequency) axis by an array of electrodes that correspond to different sound frequency bands. A major limitation of eCIs is the wide spread of electrical current in the cochlea due to the conductive fluid in the scala tympani. This limits the maximum number of perceptually different stimulation channels in the implant to typically <10, thus leading to a poor understanding of speech in noisy environments and poor appreciation for music [2–5]. A solution to reduce the spread of neural excitation and to increase the number of independent stimulation channels is to use optical stimulation instead [6]. Light can be conveniently confined in space, therefore an optical cochlear implant (oCI) combined with cochlear optogenetics improves spectral selectivity [7,8]. Dieter et al. recorded responses from inferior colliculus of gerbils in response to different stimulation conditions – acoustic, optical, and electrical [9,10]. They showed near-physiological spectral selectivity of optical stimulation with single waveguides. Moreover, the spectral selectivity of optical stimulation from single waveguides or multichannel oCIs using μLEDs was greater than that of monopolar or bipolar electrical stimulation.

Waveguide-based and LED-based oCIs have been considered as "passive" and "active" implementations (Fig. 1 A), respectively, each of them with pros and cons [6]. LEDs are Lambertian emitters, i.e. have a broad emission profile, that reach very high power efficiencies (up to approximately 50% [11]) and generating light emission inside the cochlea reduces losses. μLEDs can be integrated into flexible carriers as required for oCI by various approaches such as flip-chip bonding on the single or multi emitter level [12,13] and transfer printing [14]. Using appropriate optics the light extraction and beam profile can be optimized [15]. While no obvious heating of the cochlea by LEDs was observed in the proof-of-concept study on multichannel LED-based oCIs [13], the key challenge is to combine hermetic and long-term stable encapsulation and mechanical flexibility. Passive oCIs employ waveguides that, dependent on the numerical aperture and outcoupling mechanism, can have Gaussian emission profiles of different width or even Lambertian emission. Waveguide arrays would be coupled to multi-beam laser diodes that can be safely encapsulated in the sealed titanium housing of the CI. Therefore, passive oCIs promise better spectral selectivity and long-term safety, yet seem less power efficient given the emitter type and losses at incoupling, transmission and outcoupling of light.

To investigate the light spread in the cochlea, optical ray-tracing models were introduced and simulated for a gerbil cochlea [9,16]
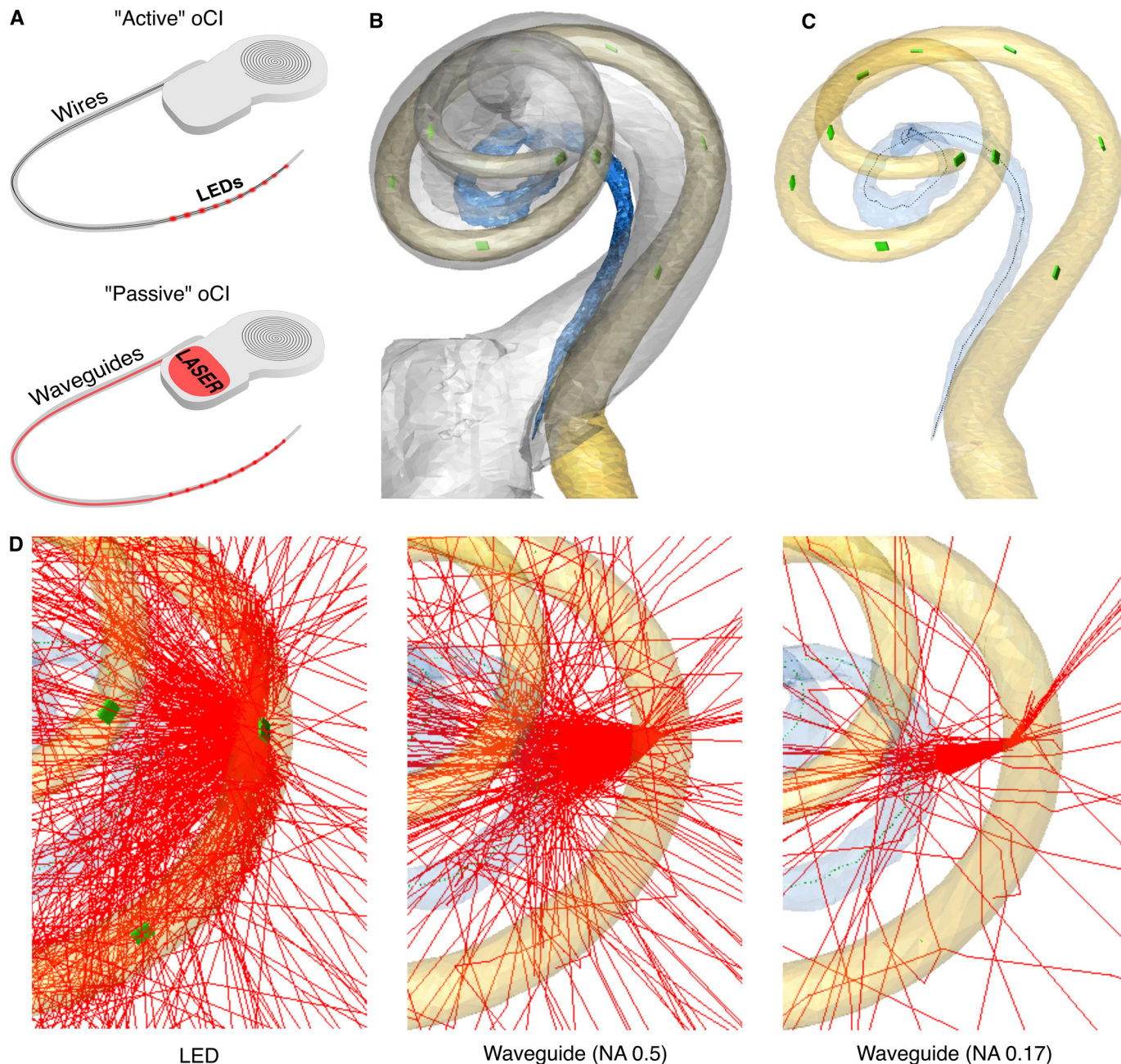

Fig. 1. Overview of the optical model framework. (A) Illustration of "active" (LED-based) and "passive" (laser-coupled waveguide-based) optical cochlear implants. Red line and dots indicate the light path. In case of "active" oCI, light is generated in the implanted array, whereas in "passive" oCI, light travels to the array through a medium, for example, a waveguide. (B) Combined model with the structures of cochlear scalae (in gray), dummy silicone implant (in yellow) sitting inside the scala tympani, and Rosenthal's canal (in blue). Bone (not shown here) was added as a cube engulfing the structures. (C) Query points (black points) at the centerline of the Rosenthal's canal, and light emitters (LEDs as green boxes) at the center of the silicone implant. (D) Exemplar ray tracing with 500 rays (in red) from the output of an LED, a waveguide with NA of 0.5, and a waveguide with NA of 0.17 (bone and scala not displayed). (For interpretation of the references to colour in this figure legend, the reader is referred to the web version of this article.)

and a marmoset cochlea [16,17] to validate the *in-vivo* stimulation. Here, we took a further step towards evaluating the potential of clinical oCIs for improved hearing restoration by investigating the spectral spread of excitation in a model of human cochlea (Fig. 1 B–D) using a range of light source parameters and comparing it to the spread of electrical current in the eCIs. Finally, we evaluated the impact of parameters relevant to the operation of oCIs – emitter-to-SGN distance, orientation of emitters, and formation of scar tissue – on the irradiance profiles.

2. Methods

2.1. Model details

TracePro Standard 7.8.1 (Lambda Research Corporation) running on Windows 10 Pro PC (Intel i7-6850 K CPU, 128 GB RAM) was used to perform Monte-Carlo ray-tracing simulation of light spread in a three-dimensional model of human cochlea. The structures of a human cochlea were reconstructed using μCT scanned images from an existing dataset [18] in Avizo (Thermo Fisher Scientific). The model consists of cochlear scalae (scala tympani as well as scalae media and vestibuli lumped into one structure), dummy silicone implant, Rosenthal's Canal (RC), bone, and multiple light emitters (Fig. 1 B–D). Published optical models of gerbil and marmoset cochleae [9,17] served as a framework for the current study.

2.2. Optical parameters

Each component of the cochlea model required certain optical properties, namely, anisotropy factor (g), scattering coefficient (μ_s), refractive index (n), absorption coefficient (μ_a), and extinction coefficient (K). Table 1 lists the values that were assigned to the different structures of the model. These values were obtained and averaged from various literature sources as the methods to measure these values vary from one study to another. Most of these values, unless calculated from wavelength-dependent equations, were observed at near-infrared region. The extinction coefficients were computed as $K = \mu_a\lambda/4\pi$, where λ is the wavelength. For simulation of cochlear fibrosis, the whole scalae structure in the model was assigned the optical properties of scar tissue.

2.3. Light sources and emitter placement

On the centerline of the silicone structure, we placed ten emitters from apex to base to study the light spread at different locations (Fig. 1 C). It is important to note that these emitters have different distances from the RC which may result in varying irradiance levels. Physical dimensions and radiation pattern of the Lambertian LEDs were obtained from the manufacturer datasheet of Cree TR2227. The laser-coupled waveguides were modelled with a diameter of 10 μm, and Gaussian radiation pattern with numerical aperture (NA) of 0.17 or 0.5. The emitting surface of each emitter faced towards the closest surface of the RC and projected three million rays at a wavelength of 655 nm (Fig. 1 D). To obtain the incident irradiance values at the RC, we placed 300 query points along the centerline of the RC (Fig. 1 C, black points). To provide an outlook on implants with greater number of channels, we generated models with 32 and 64 emitters as well. In order to evaluate the potential for improving spectral selectivity of the 64-channel oCI, the 64 emitters were placed such that they had same distance from the RC center and therefore not all of them lay inside the silicone. The query points and emitters were computationally placed using custom scripts in MATLAB R2016a (The MathWorks, Inc.).

2.4. Calculation and comparison of spectral spread

The analysis was performed with custom scripts in MATLAB R2016a (The MathWorks, Inc.). The irradiance profiles, displaying irradiance at the query points, were calculated for a radiant flux of 30 mW/emitter. Spectral spread was estimated as full width at half maximum (FWHM, see an example in Fig. 2 A2) of the irradiance profiles. This was measured in octaves by taking the base-2 logarithm of the ratio of the corresponding higher and lower frequencies (F_{high} and F_{low}, respectively, marked in Fig. 2 A2) so that for each emitter i octave was calculated as $\text{Octave}_i = \log_2(F_{i,high}/F_{i,low})$. Subsequently, the values of maximum irradiance and spectral spread were grouped in three cochlear regions: apical (<600 Hz), middle (600–2000 Hz) and basal (>2000 Hz). To compare the values of spectral spread with the current spread of eCIs, we utilized electric field imaging (EFI) data from Jürgens *et al.* [38]. They calculated FWHM of the fits to the spatial spread of electrical fields obtained from 14 participants having the same CI device and sound coding strategy. As the data did not have corresponding frequencies, we converted the values of spatial spread (in mm) to spectral spread (in octaves) by dividing the spread (in mm) by the cochlear length and multiplying with the total number of octaves. We assumed the cochlear length to be 35 mm [38] (the length of scala tympani where the EFI data was recorded) with 10 octaves so that for each emitter i octaves were calculated as $\text{Octave}_i = 3.5 \times \text{FWHM}_i$.

Table 1
Values used for optical properties of the model structures. Anisotropy factor (g), scattering coefficient (μ_s), refractive index (n), and absorption coefficient (μ_a).

Structure	g	μ_s (mm^{-1})[e] at different wavelengths				n	μ_a (mm^{-1})
		460 nm	488 nm	594 nm	638 nm		
Scala	0.88[a]	1.0	1.0	1.0	1.0	1.35[f]	0.016[j]
Rosenthal's canal	0.84[b]	17.3	15.7	11.5	10.2	1.37[g]	0.050[k]
Bone	0.83[c]	14.3	13.7	11.9	11.3	1.50[h]	1.290[l]
Scar tissue	0.80[d]	19.4	17.6	12.8	11.4	1.47[i]	0.200[m]

[a]Ref. [19].
[b]Mean of values for white matter, gray matter and brain from ref. [20–23].
[c]Mean of values for skull bone and cochlear bone from ref. [21,24–26].
[d]Ref. [20,27].
[e]Values were calculated using equations for brain, bone, and other fibrous tissues in ref. [21] For scala, ref. [28].
[f]Ref. [20].
[g]Mean of values for gray matter, neuron, and brain from ref. [20,29–31].
[h]Ref. [25,32].
[i]Ref. [33].
[j]Ref. [28].
[k]Mean of values for white matter, gray matter and brain from ref.[34,35].
[l]Mean of values for cochlear bone, adult skull, pig skull, and mouse skull from ref. [24,26,36,37].
[m]Mean of values for breast tissue without fibrocystic tissue, and skin dermis from ref. [34].

2.5. Statistical analysis

Statistical testing was performed using the statistics toolbox of MATLAB R2016a (The MathWorks, Inc.). The data of maximum irradiance and spectral spread for all three light sources were analyzed with one-way ANOVA. To analyze the data further in the categories of apical, middle, and basal regions, two-way ANOVA was used. ANOVA were followed by post hoc Tukey's test. In case of only two groups of data (i.e. "with" and "without" scar tissue), analysis was done using paired *t*-test.

3. Results

3.1. Simulating optical SGN stimulation with different types of emitters

In order to bridge the gap between current preclinical work and future clinical trials we turned to a model-based prediction of spectral selectivity of optogenetic sound encoding in the human cochlea. Scala tympani containing a silicone CI carrier, bone and Rosenthal's Canal (RC) of a human cochlea were reconstructed using existing μCT scanned images [18] in Avizo software following procedures previously described (Fig. 1 B–D, Methods; [9,17]). While the first in-man trial will likely employ oCIs with ≥32 channels (model predictions below), here, for analyzing basic principles, we only placed 10 emitters either along the centerline of the CI carrier (Fig. 1 C) or in a fixed distance from RC into scala tympani (for the simulation of 64 channels, Fig. 5). Monte-Carlo modeling of emitted rays were performed using TracePro software as previously described [9,17] building on published optical tissue properties (Table 1). As a conservative estimate of irradiance and spectral selectivity for optogenetic SGN stimulation, we read out the position of SGN somata (centerline of RC) rather than the peripheral neurites that project to the organ of Corti in closer proximity to scala tympani in the healthy cochlea, but are thought be lost in pathology long before the somata and central SGN axons. We employed three different oCI implementations: Lambertian emission from LEDs (Cree TR2227, i.e. "active" oCI implementation) and Gaussian emission from 10 μm waveguides with NAs of 0.5 and 0.17 (i.e. "passive" oCI implementation). These emission profiles could be seen as "worst", "standard", and "best" case scenarios of optical stimulation when considering efficiency and spectral selectivity° upon proper emitter orientation towards RC. The waveguides provided high irradiance of SGNs with medians of 21.59 and 18.24 mW/mm^2 for NAs of 0.17 and 0.5, respectively. LEDs provided significantly lower irradiance with a median of 1.52 mW/mm^2 (Fig. 2 A1–D1; ANOVA *p* = 0.001; post hoc tests *p* = 0.03 and < 0.001 for waveguide NAs of 0.5 and 0.17, respectively). The same irradiance profiles visualized at different *y*-scales, shows differences in the width of the curves between different emitter types, hence the spectral spread, can be appreciated (Fig. 2 A2–C2). We compared the median values of spectral spread of excitation using definition of apical, middle and basal regions and converting FWHM of each channel to octaves as described in Methods. Across the different tonotopic locations the median values of spectral spread of excitation with LEDs, waveguides of NA 0.5, and waveguides of NA 0.17 were 0.52, 0.3, and 0.19 octaves, respectively (Fig. 2 D2; ANOVA *p* = 0.001).

We also looked at the maximum irradiance and spectral spread for the same regions of the cochlea—apical, middle, and basal (Fig. 2 E). Higher irradiance and spectral selectivity of waveguides were consistently found in all regions. However, substantial heterogeneity of irradiance was observed across the emitters for all three implementations. Given their narrow emission profiles, NA 0.17 waveguides varied maximal irradiance the most. Spectral selectivity for LEDs was substantially poorer in the apical region than in the basal regions (*p* = 0.025).

3.2. Comparing predicted spectral selectivity of oCI to published eCI measurements

In an effort to put our simulations of optical stimulation in relation to measurement with the current state of clinical care, we turned to the results of a recent electric field imaging study [38]. We compared spectral spread of excitation averaged across the eCI electrodes to the median spectral spread of excitation obtained for optical simulation of apical, middle and basal emitters of the three different implementations (Fig. 3). The median of average spectral spread of excitation from 14 eCI participants with a 22-channel-implant was 2.28 octaves, with the medians of best candidate (with lowest median) at 1.16 and worst candidate at 3.06 octaves, respectively. The median spectral spread of excitation with the modeled oCIs was approximately 4 to 12 times lower (depending on the light source parameters). The decrease of spectral spread in oCIs compared to eCI was highly significant (*p* < 0.001).

3.3. Considering the effects of cochlear fibrosis and emitter position for oCI stimulation

Since cochlear implantation is often followed by cochlear fibrosis we investigated how buildup of scar tissue affects oCI stimulation. We modelled cochlear fibrosis by replacing perilymph of scala tympani by scar tissue (for details see Methods). We primarily observed a reduction of irradiance and to a lesser extent an increase of the spectral spread of excitation which we interpret to reflect prevailing forward scattering. Fibrosis had more severe impact for waveguides than for LEDs. The median value of maximum irradiance with LEDs decreased from 1.52 to 0.60 mW/mm2 (Fig. 4 A; *p* = 0.009) and the spectral spread of excitation increased from 0.52 to 0.58 octaves (Fig. S1 A). For NA 0.5 waveguides spectral spread increased from 0.3 to 0.6 octaves (Fig. S1 B; *p* = 0.03) and irradiance decreased from 18.24 to 2.04 mW/mm^2 (Fig. S1 C; *p* < 0.001).

Next, we investigated the effects of emitter-to-RC distance and orientation of the emitters. As expected, the irradiance values followed the inverse-square law of optics when we exemplarily shifted emitter 5 by 0.2 mm towards or away from the RC (Fig. 4 B). Changing emitter orientation most prominently affected NA 0.17-waveguides than LEDs (Fig. 4 C). Due to the sharp Gaussian profile of these waveguides, the irradiance decreased sharply when the orientation of the emitter 5 was changed by ± 30° relative to the direct vector from emitter surface to the RC.

3.4. Upscaling the number of oCI channels

Reduced spectral spread of oCI enables implementation of greater number of independent stimulation channels. We explored the potential for upscaling this number, as future waveguide-based oCIs will likely employ ≥32 channels to cover the physiologically available 24 critical bands [39]. We run simulations to obtain
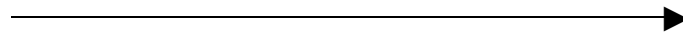
Fig. 2. Comparison of irradiance profiles, maximum irradiance, and spectral spread for LED and waveguide emitter arrays. (A–C) Irradiance profiles along the tonotopic axis, for LEDs (Lambertian-profile active light sources), laser-coupled waveguides (Gaussian-profile passive light sources) with NA of 0.5 and 0.17, with same *y*-scale (A1, B1, C1), and with *y*-scales adjusted to maximal irradiance reached with a given emitter (A2, B2, C2). Different colors represent the ten different emitters. (D) Quantification of maximum irradiance (D1) and spectral spread (D2) of LEDs and waveguides. The spectral spread in octaves was determined by taking base-2 logarithm of ratio of high and low frequencies (F_{high}/F_{low}) corresponding to the full width at half maximum (FWHM, as indicated for 10th emitter in A2). (E) Categorization of maximum irradiance (E1) and spectral spread (E2) into three cochlear regions – apical, middle, and basal. Box plots indicate median (center line), as well as 25th percentile and 75th percentile as the bottom and top edges. The whiskers extend to the maximum and minimum data points not considered outliers. The asterisks represent statistical significance (* indicates *p* < 0.05, ** indicates *p* < 0.01, and *** indicates *p* < 0.001).
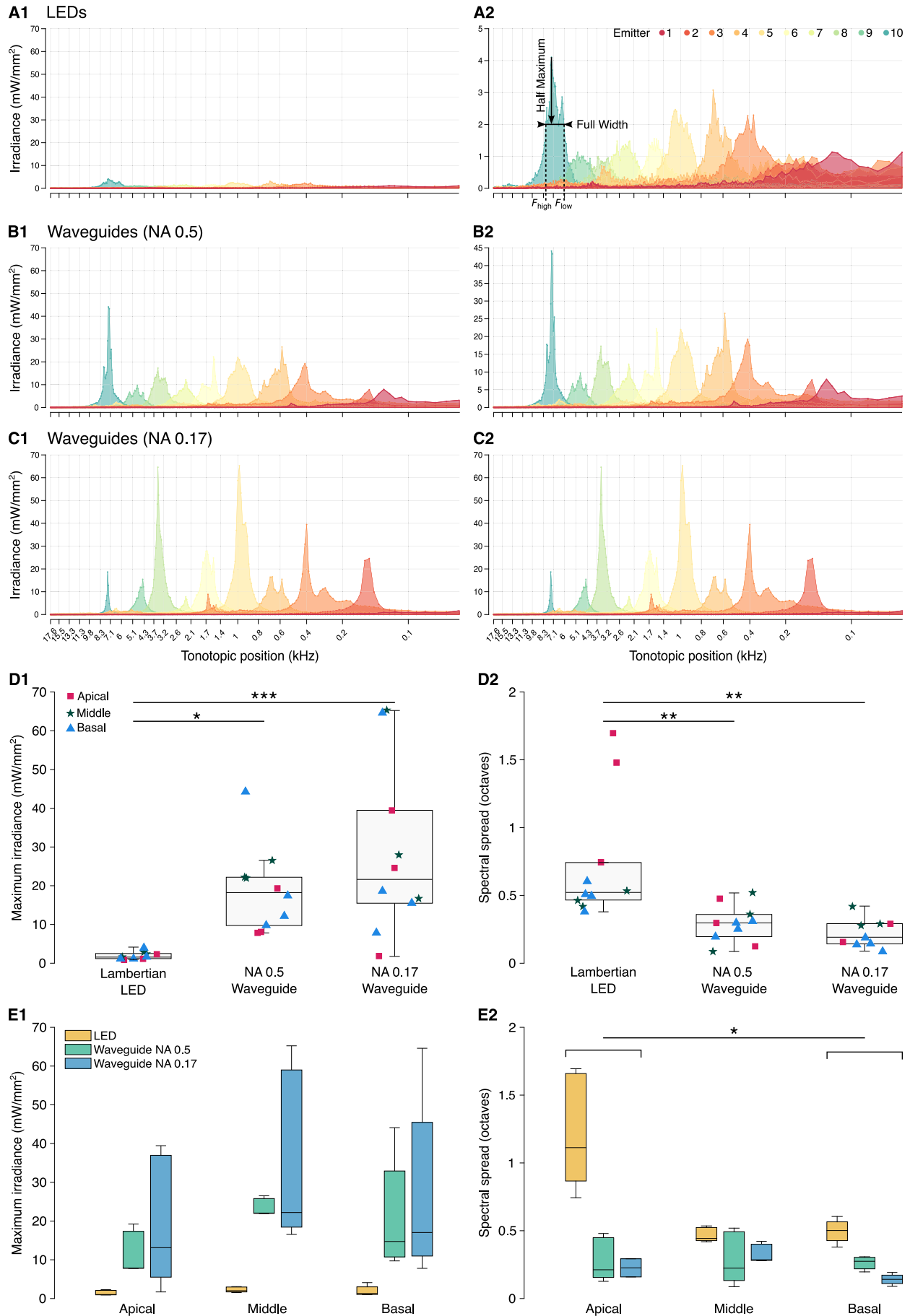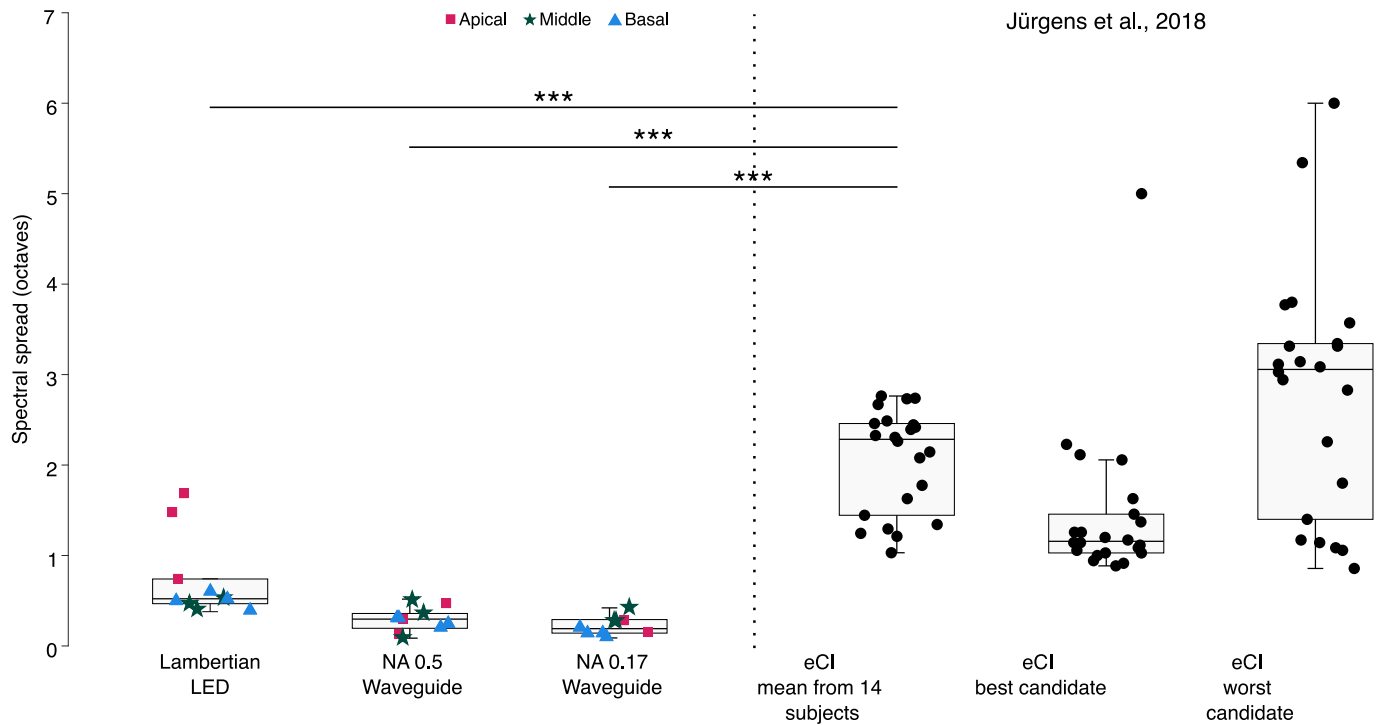
Fig. 3. Comparison of spectral spread in the cochlea from LEDs, waveguides and eCIs. (Left) Spectral spread of LEDs and waveguides as shown in Figure 2 D2. (Right) Spectral spread for eCIs from electrical field imaging of 14 subjects, each with 22-channel implant having same CI processor and sound coding strategy. The data of spatial spread (in mm) was obtained from Jürgens et al. [38] and converted to the spectral spread (in octaves) by assuming the cochlea length to be 35 mm with 10 octaves. The box plots of "best" and "worst" candidate show data from the participants with lowest and highest median spectral spread, respectively. Box plots indicate median (center line), as well as 25th percentile and 75th percentile as the bottom and top edges. The whiskers extend to the maximum and minimum data points not considered outliers. The asterisks represent statistical significance (* indicates $p < 0.05$, ** indicates $p < 0.01$, and *** indicates $p < 0.001$). The statistical comparison was performed for all three light sources with the mean eCI data only, therefore, lack of significance markers between groups does not imply insignificance.
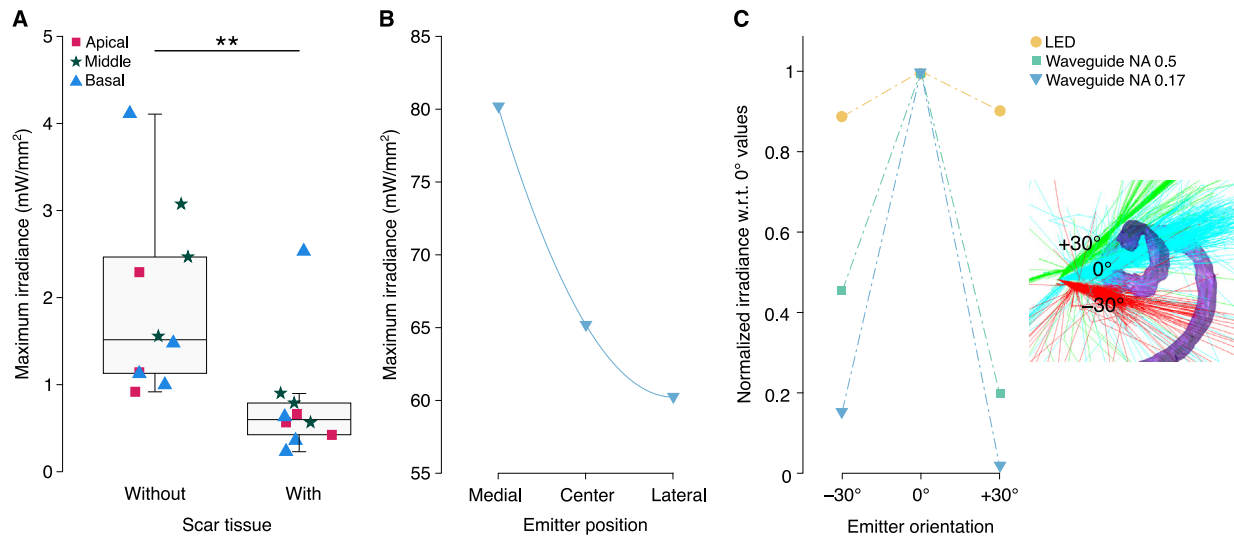

Fig. 4. Effect of fibrosis, emitter distance and emitter orientation on maximum irradiance values. (A) Impact of fibrosis (scar tissue formation) in the LED model. (B) Shift of medial–lateral position of a waveguide emitter (NA 0.17) by ± 0.2 mm, resulting in an inverse-square curve. (C) Decrease of irradiance for all three light sources with change of angle towards the RC by ± 30°. Ray tracing with the change of orientation for waveguide (NA 0.17) is displayed on the right. Box plots indicate median (center line), as well as 25th percentile and 75th percentile as the bottom and top edges. The whiskers extend to the maximum and minimum data points not considered outliers. The asterisk represents statistical significance (* indicates $p < 0.05$, ** indicates $p < 0.01$, and *** indicates $p < 0.001$). Data in (B) and (C) were not analyzed for significance due to limited number of data points.

the irradiance profiles with 32 and 64 waveguide emitters of NA 0.5 (Fig. 5). For the sake of the 64-channel simulation, we maintained a fixed emitter-to-RC distance (approximately 0.56 mm) in order to minimize differences in irradiance between the channels. The estimated irradiance values were higher than with the emitter placement followed the centerline of the silicone structure in our previous models.

4. Discussion

The present study was designed to predict the spread of light emitted from oCIs in a human cochlea. Our optical ray-tracing simulations covered different emission profiles, orientations, and positions of the emitters as well as cochlear fibrosis. Our hypothesis was that the spectral spread of SGN excitation is lower with optical
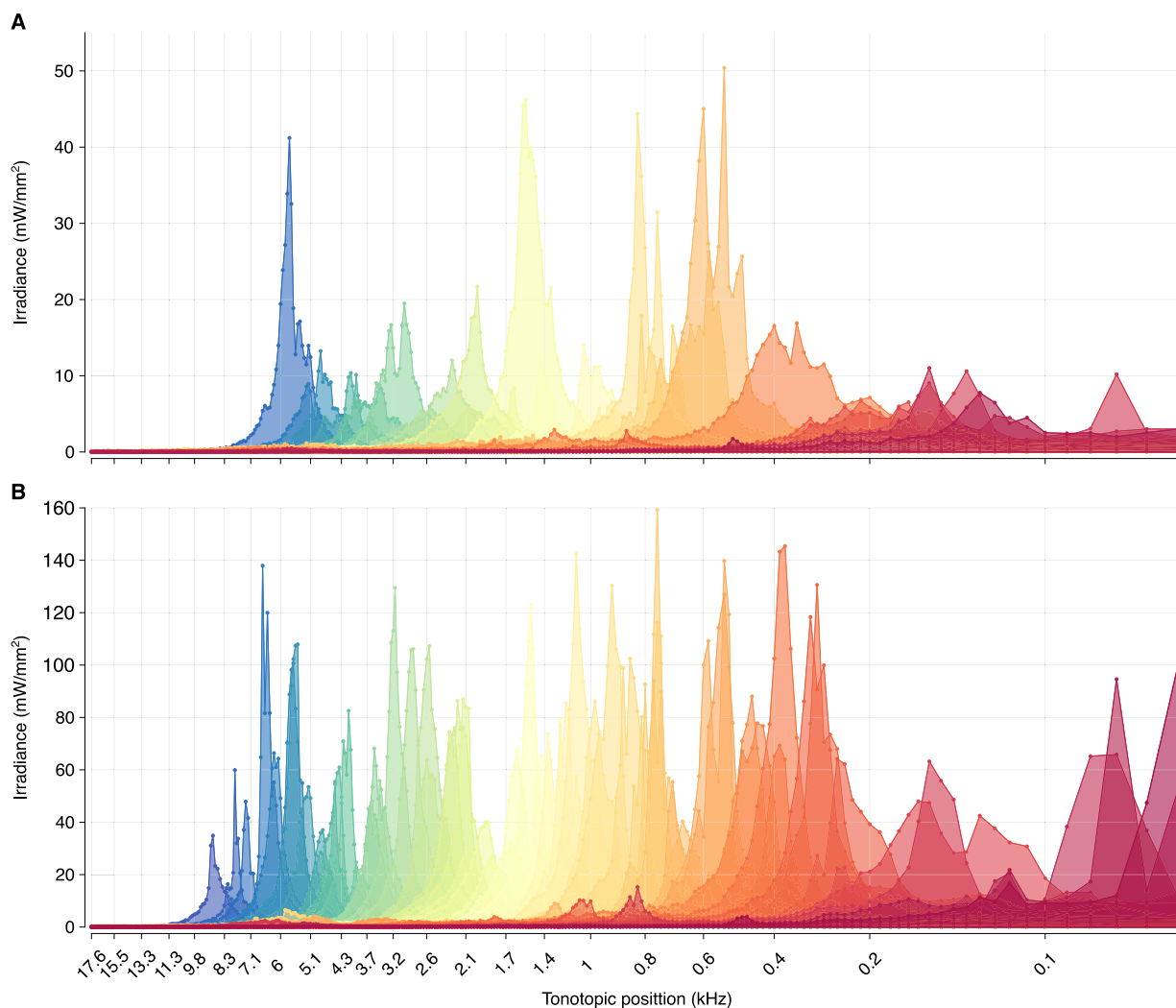
Fig. 5. Irradiance profiles, along the tonotopic axis, with increased number of oCI emitters. (A) 32 waveguide-emitters with NA of 0.5 were placed in the centerline of silicone. Different colors represent the 32 different emitters. (B) 64 waveguide-emitters with NA of 0.5 placed at equal distances from the nearest RC vertex. Different colors represent the 64 different emitters.

than with electrical stimulation. We employed an optical ray-tracing model of the cochlea in an optical engineering software and placed light emitters with three different emission profiles into the scala tympani. We obtained irradiance profiles for the SGN somata in Rosenthal's canal along the tonotopic axis. Moreover, we estimated the spectral spread of excitation for the different oCI implementations and compared it to the electrical current spread in eCIs. Finally, we scaled up the optical model to cover the large number of stimulation channels foreseen in future clinical trials. Our modeling confirms the expected improvement of spectral selectivity in oCI compared to eCI. Irradiance and spectral selectivity were weaker, the broader the emission angle. In contrast, broad angle stimulation was less susceptible to losses due to attenuation by cochlear fibrosis and mismatched emitter orientation.

4.1. Evaluating the properties of optical stimulation en route to clinical trials

Proof-of-concept animal studies have indicated feasibility of optogenetic hearing restoration [13,40–42] with improved spectral selectivity and dynamic range [9,10,13,43]. Experimental evaluation of spectral spread of cochlear excitation typically employs recordings from the tonotopically layered inferior

colliculus [9,44,45]. Using optogenetic stimulation by waveguide-based "passive" oCIs (200 μm, NA 0.39) of the gerbil cochlea in comparison to clinical-style rodent eCI and acoustic stimulation, a near physiological spectral selectivity outperforming monopolar and bipolar electrical stimulation was demonstrated [9]. The experimental average estimates of spectral spread of excitation ranged from approximately 1 octave for soft stimulation to 3 octaves for strong stimulation. Similar results were obtained with multichannel μLED-based "active" oCIs also in gerbils [10,13]. Given that the size of the gerbil cochlea is approximately a third of the human one, these results likely underestimated the spectral selectivity of optogenetic excitation in the human cochlea. The present study, therefore, aimed to obtain first predictions for optogenetic stimulation of the human cochlea. The model followed the framework of Monte Carlo ray-tracing simulations performed by Dieter et al. and Keppeler et al [9,17]. These studies used the models of gerbil and marmoset cochleae to evaluate the spectral spread at threshold levels obtained from *in-vivo* experiments in gerbils. While it was a reasonable approach to compare the spread at the threshold values, it constrained the study to the radiant flux used in these studies. Instead, here, we calculated FWHM which is independent of the radiant flux

due to the linear nature of the irradiances and does not require a fixed threshold to be set, which simplifies comparison with the literature values of current spread.

Our study confirmed the intuitive notion that Gaussian-profile waveguides are more suitable candidates than Lambertian-profile LEDs for use in an emitter array in oCIs, as they provide higher irradiance for the same radiant flux and lower spectral spread. This is an important result, keeping in mind the other benefits of using a "passive" emitter array, as mentioned in the introduction. Another finding was that the LEDs resulted in higher spectral spread in apical region than in middle or basal regions. Such wider excitation in apex than other regions has been previously reported for electrical stimulation [46–49].

Moreover, in an effort to evaluate the potential of oCIs for clinical translation, we investigated some factors which could negatively impact optogenetic stimulation. Firstly, cochlear fibrosis in response to CI implantation is known to negatively affect eCI performance and might as well hamper oCI function. In eCI cochlear fibrosis increases impedance for electrical stimulation. This decreases dynamic range as well as increases energy consumption and spectral spread [50–52]. We simulated our model in a worst-case scenario where all the scalae were filled with scar tissue. We found that the irradiance at the SGNs decreased, which would lead to the same impact, i.e., decreased dynamic range and increased energy consumption. However, the spectral spread was not significantly impacted even in this worst-case simulation. Secondly, for eCIs, increased electrode-to-SGN distance has been demonstrated to have negative impact in previous studies using computational models [53–55] and electrically-evoked compound action potential recordings [56], in similar ways as fibrosis. Since, for oCIs, the intensity of light decreases with increasing distance from emitter, the only possible solution to counter the effect is to decrease the emitter-to-SGN distance (see below). Thirdly, as the spectral spread gets narrower with oCIs, it needs to be better aligned towards the target SGNs. A trade-off might be necessary between narrower spectral spread and the loss of irradiance due to misaligned orientation.

For all these aspects, advancements in cochlear implant design and surgical techniques will greatly improve the efficiency of optical stimulation. For example, studies involving release of corticosteroids in the cochlea have shown promising results towards decreasing formation of scar tissue [57–59]. Perimodiolar (or "modiolus-hugging") implants, which are designed to lie in closer proximity to the SGNs, provide more reliable stimulation with less spectral spread [60,61]. New implantation techniques, involving imaging to plan a safe trajectory preoperatively and robotics for precise insertion, have also indicated benefits [62,63].

4.2. Comparison to the state of the art

When compared to the current spread measured using electrical field imaging in a previous study [38], all three light sources showed substantial improvement in spectral selectivity confirming our hypothesis. These results are in agreement with the electrophysiological findings of Dieter et al. which showed that the spread of excitation is more confined with optical stimulation than with electrical stimulation [9]. We note that this comparison seems valid only as a first approximation: electric field imaging does not read out the stimulation profile at the level of SGNs, which is what we employed for optical simulations. While we do not know precisely how these estimated fields relate to SGN excitation and the spread of optogenetic SGN excitation also depends on their light sensitivity, we assume it to be a good approximation for the sake of our comparison.

5. Limitations and future directions

This computational approach rests on the validity of optical parameters and together with further limitations discussed above can only provide a first approximation of what we can expected for oCI stimulation of the human cochlea. Finally, it seems difficult if not impossible to relate the estimated spectral selectivity to audiological outcomes such as speech recognition in background noise. Future studies to predict speech perception of potential oCI users and compare it with that of eCI users should combine optical modelling with a sound coding strategy, a biophysical model of SGN firing, and an objective intelligibility measure. The modelling studies presented here represent simplification of a much more complex system, nevertheless, these lay the groundwork for future research into the design and evaluation of emitter arrays and sound coding strategy for future clinical oCI system. In conclusion, this study strengthens the idea that oCI would provide improved sound perception by reducing the spectral spread, provided that the translational aspects are considered for the design of the implants.

Declaration of Competing Interest

The authors declare that they have no known competing financial interests or personal relationships that could have appeared to influence the work reported in this paper.

Author contributions

L.K., L.J., and T.M. designed the study. L.K. performed computation modeling and data analysis under supervision of L.J. and T.M., while D.K. reconstructed the 3D structures from µCT-scanned data. L.K., L.J., and T.M. designed the figures. L.K., L.J. prepared the figures. L.K., L.J., and T.M. prepared the manuscript. All authors discussed the results and commented on the manuscript.

Appendix A. Supplementary data

Supplementary data to this article can be found online at https://doi.org/10.1016/j.csbj.2022.06.061.

References

[1] World Health Organization. World report on hearing [Internet]. Geneva: World Health Organization; 2021. Available at: https://apps.who.int/iris/handle/10665/339913.

[2] Fishman KE, Shannon RV, Slattery WH. Speech recognition as a function of the number of electrodes used in the SPEAK cochlear implant speech processor. J. Speech Lang. Hear. Res. 1997;40:1201–15.

[3] Friesen LM, Shannon RV, Baskent D, Wang X. Speech recognition in noise as a function of the number of spectral channels: comparison of acoustic hearing and cochlear implants. J. Acoust. Soc. Am. 2001;110:1150–63.

[4] Zeng FG. Challenges in improving cochlear implant performance and accessibility. IEEE Trans Biomed Eng 2017;64:1662–4.

[5] Prevoteau C, Chen SY, Lalwani AK. Music enjoyment with cochlear implantation. Auris Nasus Larynx 2018;45:895–902.

[6] Dombrowski T, Rankovic V, Moser T. Toward the optical cochlear implant. Cold Spring Harb Perspect Med 2019;9:a033225.

[7] Weiss R, Voss A, Hemmert W. Optogenetic stimulation of the cochlea—critical mechanisms and first models. In 2017.

[8] Moser T, Dieter A. Towards optogenetic approaches for hearing restoration. Biochem Biophys Res Commun 2020;527:337–42.

[9] Dieter A, Duque-Afonso CJ, Rankovic V, Jeschke M, Moser T. Near physiological spectral selectivity of cochlear optogenetics. Nat Commun 2019;10:1962.

[10] Dieter A, Klein E, Keppeler D, et al. µLED-based optical cochlear implants for spectrally selective activation of the auditory nerve. EMBO Mol Med 2020: e12387.

[11] Laubsch A, Sabathil M, Baur J, Peter M, Hahn B. High-power and high-efficiency InGaN-based light emitters. IEEE Trans Electron Devices 2010;57:79–87.

[12] Gossler C, Bierbrauer C, Moser R, et al. GaN-based micro-LED arrays on flexible substrates for optical cochlear implants. J Phys D Appl Phys 2014;47:205401.

[13] Keppeler D, Schwaerzle M, Harczos T, et al. Multichannel optogenetic stimulation of the auditory pathway using microfabricated LED cochlear implants in rodents. Sci Transl Med 2020;12:eabb8086.

[14] Kim TI, McCall JG, Jung YH, et al. Injectable, cellular-scale optoelectronics with applications for wireless optogenetics. Science 2013;340:211–6.

[15] Klein E, Kaku Y, Paul O, Ruther P. Flexible µLED-based optogenetic tool with integrated µ-Lens array and conical concentrators providing light extraction improvements above 80%. In: 2019 IEEE 32nd International Conference on Micro Electro Mechanical Systems (MEMS). Seoul, 2019.

[16] Duque Afonso CJ. Development and Application of Tools for the Characterization of the Optogenetics Stimulation of the Cochlea. 2020 [cited 9 February 2021]; Available at: https://ediss.uni-goettingen.de/handle/21.11130/00-1735-0000-0005-1424-C.

[17] Keppeler D, Kampshoff CA, Thirumalai A, et al. Multiscale photonic imaging of the native and implanted cochlea. PNAS [Internet]. 2021 [cited 29 April 2021]; 118. Available at: https://www.pnas.org/content/118/18/e2014472118.

[18] Reyes M. The HEAR-EU Multiscale Imaging and Modelling Dataset of the Human Inner Ear [Internet]. SICAS Medical Image Repository; 2017. Available at: https://www.smir.ch/objects/204388.

[19] Heiskala J, Nissilä I, Neuvonen T, Järvenpää S, Somersalo E. Modeling anisotropic light propagation in a realistic model of the human head. Appl Opt 2005;44:2049.

[20] Tuchin VV. Tissue Optics: Light Scattering Methods and Instruments for Medical Diagnosis [Internet]. Society of Photo-Optical Instrumentation Engineers (SPIE); 2015 [cited 12 October 2018]. Available at: http://ebooks.spiedigitallibrary.org/book.aspx?doi=10.1117/3.1003040.

[21] Jacques SL. Optical properties of biological tissues: a review. Phys Med Biol 2013;58:R37–61.

[22] Yavari N, Dam JS, Antonsson J, Wårdell K, Andersson-Engels S. In vitro measurements of optical properties of porcine brain using a novel compact device. Med Biol Eng Compu 2005;43:658–66.

[23] Bernstein JG, Han X, Henninger MA, et al. Prosthetic systems for therapeutic optical activation and silencing of genetically-targeted neurons. Proc Soc Photo Opt Instrum Eng 2008;6854:68540H.

[24] Okamoto Ugnell A, På Ö. The optical properties of the cochlear bone. Med Eng Phys 1997;19:630–6.

[25] Niemz MH. Laser-tissue interactions: fundamentals and applications. Springer; 2007.

[26] Firbank M, Hiraoka M, Essenpreis M, Delpy DT. Measurement of the optical properties of the skull in the wavelength range 650–950 nm. Phys Med Biol 1993;38:503–10.

[27] Bashkatov A, Genina E, Kochubey V, Tuchin V. Optical properties of human sclera in spectral range 370–2500 nm. Opt Spectrosc 2010;109:197–204.

[28] Steinbrink J. Nahinfrarotspektroskopie am Kopf des Erwachsenen mit Pikosekunden-Zeitaufloeosung. 2000.

[29] Rappaz B, Marquet P, Cuche E, Emery Y, Depeursinge C, Magistretti PJ. Measurement of the integral refractive index and dynamic cell morphometry of living cells with digital holographic microscopy. Opt Express 2005;13:9361.

[30] Gottschalk W. Ein Messverfahren zur Bestimmung der optischen Parameter biologischer Gewebe in vitro [Internet] [University Dissertation]. Karlsruhe; 1992. Available at: https://services.bibliothek.kit.edu/primo/start.php?recordid=KITSRC034605355.

[31] Lue N, Bewersdorf J, Lessard MD, et al. Tissue refractometry using Hilbert phase microscopy. Opt Lett 2007;32:3522.

[32] Ye Q, Wang J, Deng Z-C, Zhou W-Y, Zhang C-P, Tian J-G. Measurement of the complex refractive index of tissue-mimicking phantoms and biotissue by extended differential total reflection method. J Biomed Opt 2011;16:097001.

[33] Tuchin VV. Optical Clearing of Tissues and Blood [Internet]. 1000 20th Street, Bellingham, WA 98227-0010 USA: SPIE; 2005 [cited 1 March 2022]. Available at: http://link.aip.org/link/doi/10.1117/3.637760.

[34] Van der Zee P. Measurement and modelling of the optical properties of human tissue in the near infrared [Internet] [Doctoral]. Doctoral thesis, UCL (University College London). UCL (University College London); 1992. Available at: https://discovery.ucl.ac.uk/id/eprint/10104457/.

[35] Patterson MS, Wilson BC, Feather JW, Burns DM, Pushka W. The measurement of dihematoporphyrin ether concentration in tissue by reflectance spectrophotometry. Photochem Photobiol 1987;46:337–43.

[36] Bevilacqua F, Piguet D, Marquet P, Gross JD, Tromberg BJ, Depeursinge C. In vivo local determination of tissue optical properties: applications to human brain. Appl Opt 1999;38:4939.

[37] Soleimanzad H, Gurden H, Pain F. Optical properties of mice skull bone in the 455- to 705-nm range. J Biomed Opt 2017;22:010503.

[38] Jürgens T, Hohmann V, Büchner A, Nogueira W. The effects of electrical field spatial spread and some cognitive factors on speech-in-noise performance of individual cochlear implant users—A computer model study. PLoS ONE 2018;13:e0193842.

[39] Zwicker E. Subdivision of the Audible Frequency Range into Critical Bands (Frequenzgruppen). The Journal of the Acoustical Society of America. 1961; 33: 248–248.

[40] Hernandez VH, Gehrt A, Reuter K, et al. Optogenetic stimulation of the auditory pathway. J Clin Invest 2014;124:1114–29.

[41] Wrobel C, Dieter A, Huet A, et al. Optogenetic stimulation of cochlear neurons activates the auditory pathway and restores auditory-driven behavior in deaf adult gerbils. Sci Transl Med 2018;10:eaao0540.

[42] Mager T, Lopez de la Morena D, Senn V, et al. High frequency neural spiking and auditory signaling by ultrafast red-shifted optogenetics. Nat Commun 2018;9:1750.

[43] Bali B, Lopez de la Morena D, Mittring A, et al. Utility of red-light ultrafast optogenetic stimulation of the auditory pathway. EMBO Mol Med 2021: e13391.

[44] Snyder RL, Bierer JA, Middlebrooks JC. Topographic spread of inferior colliculus activation in response to acoustic and intracochlear electric stimulation. J Assoc Res Otolaryngol 2004;5:305–22.

[45] Richter C-P, Rajguru SM, Matic AI, et al. Spread of cochlear excitation during stimulation with pulsed infrared radiation: inferior colliculus measurements. J Neural Eng 2011;8:056006.

[46] Mangado N, Pons-Prats J, Coma M, et al. Computational Evaluation of Cochlear Implant Surgery Outcomes Accounting for Uncertainty and Parameter Variability. Frontiers in Physiology [Internet]. 2018 [cited 2 February 2022]; 9. Available at: https://www.frontiersin.org/article/10.3389/fphys.2018.00498.

[47] van der Beek FB, Briaire JJ, van der Marel KS, Verbist BM, Frijns JHM. Intracochlear position of cochlear implants determined using CT scanning versus fitting levels: higher threshold levels at basal turn. AUD 2016;21:54–67.

[48] Biesheuvel JD, Briaire JJ, Frijns JHM. A novel algorithm to derive spread of excitation based on deconvolution. Ear Hear 2016;37:572–81.

[49] Briaire JJ, Frijns JHM. The consequences of neural degeneration regarding optimal cochlear implant position in scala tympani: a model approach. Hear Res 2006;214:17–27.

[50] Kawano A, Seldon HL, Clark GM, Ramsden RT, Raine CH. Intracochlear factors contributing to psychophysical percepts following cochlear implantation. Acta Otolaryngol 1998;118:313–26.

[51] Wilk M, Hessler R, Mugridge K, et al. Impedance changes and fibrous tissue growth after cochlear implantation are correlated and can be reduced using a dexamethasone eluting electrode. PLoS ONE 2016;11:e0147552.

[52] Ni D, Shepherd RK, Seldon HL, Xu SA, Clark GM, Millard RE. Cochlear pathology following chronic electrical stimulation of the auditory nerve. I: Normal hearing kittens. Hear Res 1992;62:63–81.

[53] Yang H, Won JH, Choi I, Woo J. A computational study to model the effect of electrode-to-auditory nerve fiber distance on spectral resolution in cochlear implant. PLoS ONE 2020;15:e0236784.

[54] Goldwyn JH, Bierer SM, Bierer JA. Modeling the electrode–neuron interface of cochlear implants: effects of neural survival, electrode placement, and the partial tripolar configuration. Hear Res 2010;268:93–104.

[55] Mino H, Rubinstein JT, Miller CA, Abbas PJ. Effects of electrode-to-fiber distance on temporal neural response with electrical stimulation. IEEE Trans Biomed Eng 2004;51:13–20.

[56] DeVries L, Scheperle R, Bierer JA. Assessing the electrode-neuron interface with the electrically evoked compound action potential, electrode position, and behavioral thresholds. J Assoc Res Otolaryngol 2016;17:237–52.

[57] Lyu A-R, Kim DH, Lee SH, Shin D-S, Shin S-A, Park Y-H. Effects of dexamethasone on intracochlear inflammation and residual hearing after cochleostomy: A comparison of administration routes. Eshraghi AA, Ed. PLoS ONE 2018;13:e0195230.

[58] Toulemonde P, Risoud M, Lemesre PE, et al. Evaluation of the efficacy of dexamethasone-eluting electrode array on the post-implant cochlear fibrotic reaction by three-dimensional immunofluorescence analysis in mongolian gerbil cochlea. J Clin Med 2021;10:3315.

[59] Liebau A, Schilp S, Mugridge K, et al. Long-Term in vivo Release Profile of Dexamethasone-Loaded Silicone Rods Implanted Into the Cochlea of Guinea Pigs. Frontiers in Neurology [Internet]. 2020 [cited 1 March 2022]; 10. Available at: https://www.frontiersin.org/article/10.3389/fneur.2019.01377.

[60] Roland JT. A model for cochlear implant electrode insertion and force evaluation: results with a new electrode design and insertion technique. Laryngoscope 2005;115:1325–39.

[61] Hughes ML, Abbas PJ. Electrophysiologic channel interaction, electrode pitch ranking, and behavioral threshold in straight versus perimodiolar cochlear implant electrode arrays. J Acoust Soc Am 2006;119:1538–47.

[62] Auinger AB, Dahm V, Liepins R, Riss D, Baumgartner W-D, Arnoldner C. Robotic Cochlear Implant Surgery: Imaging-Based Evaluation of Feasibility in Clinical Routine. Frontiers in Surgery [Internet]. 2021 [cited 1 March 2022]; 8. Available at: https://www.frontiersin.org/article/10.3389/fsurg.2021.742219.

[63] Panara K, Shahal D, Mittal R, Eshraghi AA. Robotics for cochlear implantation surgery: challenges and opportunities. Otol Neurotol 2021;42. e825–e835.